Directly Measured Heating Rates of a Tropical Subvisible Cirrus Cloud

Anthony Bucholtz[1*], Dennis L. Hlavka[2], Matthew J. McGill[3], K. Sebastian Schmidt[4], Peter Pilewskie[4], Sean M. Davis[5], Elizabeth A. Reid[1], and Annette L. Walker[1]

[1]Naval Research Laboratory, Monterey, CA

[2]Science Systems and Applications, NASA Goddard Space Flight Center, Greenbelt, MD

[3]NASA Goddard Space Flight Center, Greenbelt, MD

[4]University of Colorado, Boulder, CO

[5]NOAA Earth System Research Laboratory, Boulder, CO

*Corresponding Author: Anthony Bucholtz, Marine Meteorology Division, Naval Research Laboratory, 7 Grace Hopper Ave., Stop 2, Monterey, CA 93943-5502 Tel: 831-656-5024, Fax: 831-656-4769, Email: anthony.bucholtz@nrlmry.navy.mil

Abstract

We present the first direct measurements of the infrared and solar heating rates of a tropical subvisible cirrus (SVC) cloud sampled off the east coast of Nicaragua on 25 July 2007 by the NASA ER-2 aircraft during the Tropical Composition, Cloud and Climate Coupling Experiment (TC4). On this day a persistent thin cirrus layer, with mostly clear skies underneath, was detected in real-time by the cloud lidar on the ER-2 and the aircraft was directed to profile down through the SVC. Measurements of the net broadband infrared irradiance and spectrally integrated solar irradiance above, below, and through the SVC are used to determine the infrared and solar heating rates of the cloud. The lidar measurements show that the variable SVC layer was located between ~13-15 km. Its midvisible optical depth varied from 0.01-0.1 with a mean of 0.0342 and a standard deviation of 0.0328. Its depolarization ratio was approximately 0.4, indicative of ice clouds. From the divergence of the measured net irradiances the infrared heating rate of the SVC was determined to be ~2.50-3.24 K day^{-1} and the solar heating rate was found to be negligible. These values are consistent with previous indirect observations of other SVC and with model-generated heating rates of SVC with similar optical depths. This study illustrates the utility and potential of the profiling sampling-strategy employed here. A more fully instrumented high altitude aircraft that also included in situ cloud and aerosol probes would provide a comprehensive dataset for characterizing both the radiative and microphysical properties of these ubiquitous tropical clouds.

1. Introduction

Subvisible cirrus (SVC) are high altitude, optically thin ice clouds that are very common in the tropics. They are called subvisible because they are difficult to see visually from below or above and only become apparent when viewed edge-on, as when looking towards the horizon from an airplane. As a general rule of thumb it has been estimated that a visible cloud optical depth of approximately 0.03 is the minimum threshold for visual observation of these clouds (Sassen and Cho, 1992).

The extent and prevalence of subvisible cirrus was first detected by ground based lidar measurements in the western tropical Pacific at Kwajalein Atoll in the 1970s (Uthe and Russel, 1976). Subsequent satellite (Prabhakara et al., 1993; Wang et al., 1996; Winker and Trepte, 1998; Dessler et al., 2006; Mace et al., 2009), aircraft lidar (McFarquhar et al., 2000; Pfister et al., 2001) and ground-based lidar (Comstock et al., 2002) studies have confirmed the prevalence of SVC in the tropics and found that they are present approximately 30-50% of the time depending on location. These studies have also found that the SVC are located near the tropopause at altitudes of 14-17 km and are typically less than a kilometer thick. They can be variable in space and time or they can extend for hundreds of kilometers across the sky and last for several days. SVC have been detected as a single isolated layer or as a layer above deep convection. Ground-based lidar studies have also detected subvisible cirrus at mid-latitudes (Sassen et al., 1989; Sassen and Cho, 1992; Sassen and Campbell, 2001; Immler and Schrems, 2002)

Since their discovery over thirty years ago there have only been a few direct aircraft measurements of SVC, and these have been limited to measurements of the microphysical properties of the clouds. Heymsfield (1986) performed the first in situ

measurements of SVC acquiring data on the habits and sizes of the ice crystals in the cloud from a WB-57 aircraft over Kwajalein in 1973. Since then only a few in situ aircraft microphysical measurement studies have been performed (Booker and Stickel, 1982; Peter et al., 2003; Lawson et al., 2007). More recently, Davis et al. (2010, this issue) report on aircraft in situ and lidar measurements of the microphysical properties of a subvisible cirrus made from the NASA WB-57 aircraft during the TC4 field study near Costa Rica focusing on the 6 August 2009 flight, a different SVC case than discussed in this paper.

This lack of measurements has left many uncertainties about the radiative and microphysical properties and effects of subvisible cirrus, and about their formation and persistence mechanisms. However, because of the prevalence of SVC in the tropics, several studies have suggested that these clouds may play an important role in the radiative balance of the tropical upper troposphere and in stratosphere-troposphere exchange by absorbing outgoing thermal infrared (IR) radiation and causing a subsequent modification of the thermodynamic structure of the upper troposphere (Gage et al., 1991; Jensen et al., 1996b; Rosenfield et al., 1998; Corti et al., 2006). This heating of the cloud layer may also play a role in the persistence of the SVC by either warming the cloud and causing it to dissipate in a matter of hours or by inducing a lifting of the cloud and causing it to persist for days (Jensen et al. 1996a). Two recent modeling studies have suggested that the IR heating of the SVC thermally forces a mesoscale circulation that enables the cloud to maintain itself for up to 2 days (Durran et al., 2009; Dinh et al., 2009).

To address these issues accurate estimates of the radiative heating rates of the SVC are required. Several studies have estimated SVC heating rates of a few K per day (Jensen et al., 1996a; McFarquhar et al., 2000; Comstock et al., 2002). In general, these studies estimated the heating rates with a radiativc transfer model using as input the microphysical data from the limited set of in situ aircraft measurements, and optical depth and cloud boundary information from lidar measurements. Until now there has not been a direct measurement of the heating rates of subvisible cirrus to evaluate these estimates.

Here we present the first direct measurements of the infrared and solar heating rates of a tropical subvisible cirrus cloud sampled off the east coast of Nicaragua on 25 July 2007 by the NASA ER-2 aircraft during TC4. For almost the entire flight on this day the downlooking cloud lidar on the ER-2 detected a persistent subvisible cirrus layer near the bottom of the tropopause, with mostly clear skies underneath. Fortunately, the ER-2 had a satellite downlink capability during TC4 that provided real time views on the ground of the cloud lidar data showing the presence, altitude and thickness of the SVC below the aircraft. This enabled mission scientists to vector the ER-2 pilot to the proper altitudes and coordinates to profile through the cirrus layer. Measurements from this flight of the net broadband infrared irradiance and spectrally integrated solar irradiance above, below, and through the SVC are used to directly determine the infrared and solar heating rates of the cloud. In section 2 we describe the instruments on the ER-2 that were used in this study, specifically, the Broadband IR Radiometers (BBIR), the Solar Spectral Flux Radiometer (SSFR), and the Cloud Physics Lidar (CPL). In section 3 we present the meteorological conditions on this day and the morphological and optical properties of the SVC measured by the lidar. In section 4 we illustrate the aircraft profiling strategy used

to sample the SVC layer. In section 5 we present the results of our measurements of the IR and solar heating rates of the subvisible cirrus. In section 6 we compare our measurements to model generated values and in section 7 we summarize our results and make suggestions for future aircraft measurements of SVC.

2. Instrument Description

2.1. Broadband Infrared Radiometers (BBIR)

The BBIRs are Kipp & Zonen CG-4 pyrgeometers (Kipp & Zonen, 2003) that have been modified to make them better suited for use on an aircraft (Bucholtz and Jonsson, 2010). They have a hemispheric field-of-view and a wavelength bandpass of 4.5-42 μm. For TC4 identical BBIRs were mounted on the top and bottom of the ER-2 fuselage to measure the downwelling and upwelling IR irradiance, respectively.

The modifications made to these commercially available radiometers include a new back housing that retains the front end optics and electronics of the original instrument but allows an amplifier to be mounted directly below the sensor. The signal is then amplified from the milli-Volt range to the 0-10 Volt range and the instrument is run in current loop mode, a well established technique for minimizing the effects of noise in long signal cables. This technique is especially effective in the electronically noisy environment of a research aircraft. The new housing has the cable connector on the bottom of the instrument for easier mounting onto the aircraft. It is hermetically sealed and has a pop-up pressure relief valve that allows evacuation of air from inside the instrument to prevent damage or data loss due to condensation or freezing inside the instrument dome.

The Kipp & Zonen pyrgeometers have features that make them attractive for aircraft use even before modification. The off-the-shelf CG-4s have a silicon dome that acts as a solar blind filter and has an ellipse shape with a full 180° field-of-view with a good cosine response. Due to the construction methods used, any solar radiation absorbed by the window is effectively conducted away, allowing accurate measurements in full sunlight and eliminating the need for any shading disk. In addition, excellent dome to body thermal coupling eliminates the need for a dome thermistor, and the calculation of the dome to body temperature offset that is required by other pyrgeometers (Kipp & Zonen, 2003; Philipona et al., 1995).

The BBIRs were calibrated in-house both pre- and post-mission. The calibration entailed having the BBIRs view a blackbody source whose temperature was varied. The calibration constants were then derived from a fit of the known blackbody irradiance at each temperature versus the raw BBIR signal (in Volts). The pre- and post-mission calibrations agreed to within 5% for the downlooking radiometer and to within 2% for the uplooking radiometer, showing the stability of the BBIRs over the course of TC4.

As an additional test, side-by-side comparisons of the up- and down-looking BBIRs used on the ER-2 were done outside under varying sky conditions. This comparison is especially important for this study because we use the net flux, or difference between the up- and down-looking radiometer measurements, in the determination of SVC heating rates. The relative error between the two instruments is therefore more important than the absolute error of each. The side-by-side comparisons showed that the two BBIRs agreed to within +/- 1.0%. Based on these calibrations and tests the accuracy of the BBIRs is estimated to be 2-5% and the precision is estimated to be 1-3%.

2.2 Solar Spectral Flux Radiometer (SSFR)

The SSFR (Pilewskie et al., 2003) consists of two spectroradiometers connected via fiber optic cables to optical inlets containing a miniature integrating sphere for light collection. An optical inlet was mounted on the top (zenith viewing) and bottom (nadir viewing) of the NASA ER-2 fuselage for TC4 to measure the downwelling and upwelling spectrally resolved solar irradiance, respectively. The wavelength range of the instrument, 350 to 2150 nm, encompasses 90% of incident solar radiation. This wavelength range is covered by using two spectrometers per optical inlet: a grating spectrometer with a Silicon Charged Coupled Device (CCD) array for near-ultraviolet, visible and very near-infrared (350-1000 nm, 8 nm spectral resolution) and a spectrometer with an Indium-Gallium-Arsenide linear array detector for the shortwave infrared (900-2200 nm, 12 nm resolution) wavelength range. The SSFR records a nadir and zenith spectrum every second. For the calculations of solar heating rates discussed in this paper the SSFR data was integrated over its wavelength range to give the broadband downwelling and upwelling solar irradiance.

The spectrometers are calibrated in the laboratory with a National Institute of Standards and Technology (NIST)-traceable blackbody (tungsten-halogen 1000W bulb). The radiometric stability of the SSFR is carefully tracked during the course of a field experiment with a portable field calibration unit with a highly stable power source and 200W lamps. The calibration held to the 1 to 2% level over the course of the TC4 field mission. The radiometric calibration was adjusted for minor fluctuations measured by the field calibration from flight to flight.

The data were corrected for the angular response of the light collectors and for deviations of the light collector reference plane (SSFR horizon) from horizontal due to changes in aircraft attitude (pitch, roll, and heading) which can introduce artificial offsets into the measurements of the downwelling solar irradiance. No active stabilization of the radiometers was available for this experiment. Prior to correction, the data are filtered such that measurements with only moderate deviations from horizontal alignment (less than 3°) are used. The downwelling solar radiation is then corrected for any tilt in the instruments by scaling the direct component of the solar radiation by the ratio of the cosine of the true solar zenith angle (determined from ephemeris data) to the cosine of the solar zenith angle with respect to the instrument (determined from the aircraft pitch, roll, and heading), and assuming an isotropic radiance distribution for the diffuse component of the solar radiation. The direct-diffuse ratio of solar radiation is estimated using a radiative transfer code - a good approximation at the high altitudes of the ER-2 where there is very little diffuse and the direct component of solar radiation dominates the diffuse component. Schmidt et al., (2010, this issue) estimate a combined systematic error in the downwelling solar irradiance (radiometric uncertainty, angular response, and attitude correction) of 7%, and an error in the upwelling solar irradiance of 3-5% .

2.3. Cloud Physics Lidar (CPL)

The CPL is a multi-wavelength backscatter lidar built for use on the high altitude ER-2 aircraft and was first deployed in 2000 (McGill et al., 2002; 2003). It was mounted in a wing pod on the ER-2 for TC4 and looked downward. The CPL utilizes a high repetition rate, low pulse energy transmitter and photon-counting detectors. It is designed

specifically for three-wavelength operation (355, 532, and 1064 nm, with depolarization at 1064 nm) and maximum receiver efficiency. An off-axis parabola is used for the telescope, allowing 100% of the laser energy to reach the atmosphere. The CPL is designed with a nominal 100 microradian field of view to minimize the effects of multiple scattering. CPL data products are typically provided at 30 m vertical resolution and 1 second horizontal resolution (~200 m at the nominal ER-2 speed of 200 m/s). Complete instrument details can be found in McGill et al. (2002).

The CPL fundamentally measures the total (aerosol plus Rayleigh) attenuated backscatter as a function of altitude at each wavelength. Considerable data processing is required to separate backscatter from clouds and aerosol and backscatter from Rayleigh. However, for transmissive cloud/aerosol layers, using optical depth measurements determined from attenuation of Rayleigh and aerosol scattering, and using the integrated backscatter, the extinction-to-backscatter parameter (S-ratio) can be directly derived. This permits unambiguous analysis of layer optical depth since only the lidar data is required; there is no need to use other instrumentation nor is there need for assumptions of aerosol climatology. Using the derived extinction-to-backscatter ratio, the internal cloud extinction profile can then be obtained. The error in the optical depth retrieval is estimated to be 25%, while the error in the depolarization ratio retrieval is estimated to be 15%. This approach to directly solving the lidar equation without assumption is a standard analysis approach for backscatter lidar and more complete detail can be found in McGill et al. (2003).

2.4. ER-2 Satellite Downlink (REVEAL):

The TC4 mission provided an opportunity for real time flight planning and aircraft coordination. The NASA-developed Research Environment for Vehicle Embedded Analysis on Linux (REVEAL) system www.nasa.gov/centers/dryden/research/ESCD/OTH/Tools_Technologies/reveal.html was installed on all three of the NASA aircraft participating in TC4 (i.e. the ER-2, WB-57, and DC-8 aircraft). The REVEAL system permits real time reporting of the aircraft location and, more importantly, provides a means for real time downlinking of data from the aircraft instruments. The CPL onboard the ER-2 aircraft was one of the first instruments to utilize this capability of REVEAL. Although bandwidth limitations prohibited downlinking of all CPL data, the CPL profiles were temporally subsampled at ~10 second intervals and sent to the TC4 mission operations center. Real time interpretation of the CPL profiles permitted identification of subvisible cirrus layers and the aircraft could then be vectored to the correct latitude, longitude and altitude to sample the SVC.

3. Overview of 25 July 2007 ER-2 Subvisible Cirrus Case Study

Figure 1 shows the entire flight track of the ER-2 on 25 July 2007 overlayed on the Geostationary Operational Environmental Satellites (GOES) Visible image from 16:28 UTC (about midway into the flight). The altitude profile of the ER-2 is shown in the inset of the figure. For TC4 the ER-2 was based out of the Juan Santamaria Airport near San Jose, Costa Rica. On this day the ER-2 was the only TC4 aircraft flying. Figure 1 shows that, for the most part, the ER-2 flew over the apparent clear sky areas in the region avoiding the larger convective cells off the east coast of Costa Rica (except on

250 take-off and landing), and the smaller convective cell to the North off the east coast of
251 Honduras.

252 To put the radiometric and lidar measurements into context Figure 2 shows altitude
253 profiles of the temperature, wind direction, and wind speed as measured by the ER-2 on
254 its initial climb out over the Caribbean (red lines) and by balloonsondes (Vömel et al,
255 2007) launched from Alajuela, Costa Rica before (blue lines) and near the end (green
256 line) of the flight (Selkirk et al. 2010). The balloonsonde near the end of the flight at
257 17:05 UTC did not measure winds. Figure 2a shows that the bottom of the tropopause
258 was at ~15 km with a small inversion between 15-16 km. Figures 2b and 2c show the
259 winds were mostly out of the east and were stronger below the tropopause. The
260 temperature and wind data measured from the ER-2 later in the flight (not shown here) at
261 the location of the ER-2 profile through the SVC discussed in this paper (see Fig. 1) also
262 showed the bottom of the tropopause was at ~15-16 km with winds mostly out of the
263 east.

264 Figure 3 shows the CPL attenuated backscatter signal as measured from the ER-2 for
265 the entire flight on this day. A variable, but persistent thin cirrus layer located between
266 approximately 13-15 km is apparent for most of the flight even though the GOES visible
267 satellite image (Figure 1) seems to indicate mostly clear skies along the flight track. The
268 thin cirrus layer occurs just below the bottom of the tropopause as indicated in Figure 2a.
269 The lidar data also shows that except for near the convective cloud regions it was mostly
270 clear underneath this thin cirrus layer for the majority of the flight, with only scattered
271 low clouds below 4 km. The ER-2 pilot reported that he could not see this thin cirrus

layer, even when he profiled through it. It only became apparent to him when he looked towards the horizon.

Figure 4 shows the midvisible (532 nm) optical depth and depolarization ratio (at 1064 nm) derived from the lidar data for a representative section of the thin cirrus layer. The data is given for the flight segment (times: 16:20-16:39 UTC) that occurred right after the ER-2 had completed the profile down through the cirrus, climbed back up to altitude, and then reversed course, overflying the same flight track and locations of the profile. The optical depths and depolarization ratios in Figure 4 are therefore representative of the cirrus sampled during the profile. The optical depth of the cirrus layer varies between approximately 0.01 - 0.1 with a mean of 0.0342 and a standard deviation of 0.0328. These values are near or below the estimated minimum threshold for visual observation of the cloud. The measured depolarization ratio is approximately 0.4, indicative of ice clouds.

The low optical depths of these thin ice clouds and their location near the bottom of the tropopause, combined with the fact that they do not show up in the visible satellite image and they were not seen by the ER-2 pilot, are all consistent with these clouds being subvisible cirrus.

4. ER-2 Subvisible Cirrus Sampling Strategy

The ER-2 for TC4 was meant to serve as a remote sensing platform, or satellite surrogate, typically flying at a high, constant altitude of approximately 20 km. However, three factors came together in TC4 that provided an opportunity to directly measure the radiative heating rates of the subvisible cirrus by having the ER-2 deviate from its

nominal flight pattern and profile down through the cirrus layer. First, the high altitude of the SVC put them within reach of the ER-2. Second, as described in section 2.4, the ER-2 was equipped with a real-time downlooking cloud lidar that gave mission scientists on the ground the ability to direct the ER-2 to the proper coordinates and altitudes to sample the SVC. Third, the broadband IR and spectral solar irradiance radiometers on the ER-2 provided measurements of the net irradiances as a function of altitude from which the heating rates could be determined.

Figure 5 shows an idealized schematic of the flight profile flown by the ER-2 to sample the subvisible cirrus layer. On the initial northbound heading in the Caribbean (see Figure 1) the presence, altitude and thickness of the cirrus was detected in real-time by the cloud lidar (see Figure 3). At the very north end of that leg the ER-2 began to pass over a convective system off the east coast of Honduras. Therefore, the ER-2 was directed to reverse course, and once south of the convection, was given the altitudes to descend to in order to sample the previously seen SVC. As shown in Figure 5, the flight pattern consisted of a level leg above and below the cloud, and a descent and ascent through the cloud. To minimize the effects of tilt on the IR, and especially the solar, irradiance measurements (see discussion in Bucholtz et al. (2008)), the ER-2 pilot kept the attitude of the aircraft as 'flat' as possible throughout the pattern. That is, the pitch and the roll of the aircraft were kept to a minimum. For the majority of the pattern, even during the descent and climb, the pitch was kept below 2°, and the roll was kept below 1°, except during the 180° turn to reverse course at the end of the descent to below the cloud. The measurements during this 180° turn are not used in the analysis below. The ER-2 began its initial descent from 20 km at approximately 15:25 UTC and eventually returned

to its nominal altitude at approximately 16:30 UTC, so the complete "dip" maneuver into the SVC took about 65 minutes. The flight times of each leg are given in Figure 5.

5. Measured Subvisible Cirrus Heating Rates

The heating or cooling rate for a given layer in the atmosphere is defined as (Liou, 1980):

$$\left(\frac{\partial T}{\partial t}\right) = \frac{g}{c_p}\frac{\nabla F}{\Delta p} \quad (1)$$

where T=temperature (degrees Kelvin), t=time (day), g=gravitational acceleration (=980.616 cm sec^{-2}), c_p=specific heat at constant pressure (=1.004x10^7 cm^2 sec^{-2} K^{-1}), Δp is the difference in pressure between the lower and upper altitude boundaries of the given layer, and ∇F is the difference between the net irradiances at the lower and upper boundaries of the given altitude layer. The broadband IR and spectrally integrated solar net irradiances measured from the ER-2 as it profiled through the SVC layer are used here to determine the heating rates of the cloud.

Figure 6 shows the net broadband solar irradiances determined from the spectral solar measurements of the SSFR instrument on the ER-2 as it profiled through the SVC layer. The net broadband solar irradiance is defined as the difference between the downwelling and upwelling solar irradiance at a given altitude. While the SSFR is a spectral instrument we are interested here in determining the complete solar heating rate of the SVC, therefore we have integrated the SSFR signal over its complete wavelength range in order to get broadband solar irradiances. The net solar irradiance measurements shown in Figure 6 have been normalized to a common solar zenith angle of 24.162° to account for the change in downwelling solar irradiance as the sun rose in the sky during this

portion of the flight. The data have also been corrected for the attitude (pitch, roll, and heading) of the aircraft as described in section 2.2. The solar measurements during the 180° turn of the ER-2 on the below-cloud leg at ~15:48 UTC have been filtered out. The dip in the measurements near 15:44 and 15:53 correspond to a low level cloud of limited extent.

Ignoring these dips it can be seen that within the precision of the instrument there is no significant change in the net solar irradiance as the ER-2 profiles through the SVC layer. The net solar irradiance measurements for the above and below cloud legs are the same, and there is no change in the net solar as the ER-2 descends or ascends through the cloud. In effect, the SVC is not "seen" in the broadband solar irradiance data, indicating that there is no significant solar radiative energy being deposited into or out of the SVC layer. The ∇F term in Eq. (1) for this case is therefore near zero, and the solar heating rate for this SVC layer is zero or negligible.

This is not the case for the IR measurements. Figure 7 shows the net broadband IR irradiances measured by the BBIR instruments on the ER-2 as it profiled through the SVC layer. The net broadband IR irradiance is defined as the difference between the upwelling and downwelling IR irradiance at a given altitude. As we did for the solar measurements, the IR measurements during the 180° turn of the ER-2 on the below-cloud leg at about 15:48 UTC have been filtered out. The large dip in the net irradiance at approximately 15:38 UTC and the smaller dip near 15:53 UTC correspond to lower level clouds of limited extent below the SVC (also see the lidar image in Figure 3 for these times).

Ignoring these dips in the data, it can be seen that the net IR irradiance at the level leg just above the cirrus is less than the net IR irradiance at the level leg just below the cirrus, and that the net IR irradiance increases approximately linearly with decreasing altitude through the cloud. Since the primary source for thermal IR radiation in the atmosphere is the Earth's surface (i.e. from below), the fact that the net IR irradiance above the cirrus is smaller than the net IR irradiance below the cirrus indicates that IR radiative energy is being deposited into the SVC layer. This IR energy will warm the layer.

Two methods were used to estimate the IR heating rate of the SVC layer. The first method determined the heating rate from the difference in the net IR irradiance at the level leg above and below the cirrus. For this case, the measured pressure and net IR irradiance for each of the legs were averaged. For the above cloud leg the mean pressure was 113.97 mb and the mean net IR irradiance and standard deviation were 275.16 +/- 3.33 W m^{-2}. For the below cloud leg the mean pressure was 137.2 mb and the mean net IR irradiance and standard deviation were 282.03 +/- 2.33 W m^{-2}. The standard deviations of the net IR irradiances incorporate both the limits in the precision of the IR radiometers and the natural variability in the IR signal from the atmosphere. These values were put into Eq. (1) and using standard propagation of error analysis (Bevington, 1969) the IR heating rate was found to be:

$$\text{IR Heating Rate (from level legs)} = 2.50 \pm 1.48 \text{ K day}^{-1}$$

The second method for estimating the IR heating rate used the net irradiance data during the descent and ascent legs of the profile. At first glance, this would appear to be a straightforward method. Simply use Eq. (1) to calculate the heating rate profile by numerically differentiating the measured net IR irradiances with respect to pressure (i.e.

6. Comparison to Calculated Values

The heating rates measured in this paper are consistent with previous model generated values for subvisible cirrus of comparable optical depths. For example, Jensen et al. (1996a) used a detailed cirrus cloud model and the in situ microphysical aircraft measurements from Heymsfield (1986) to estimate heating rates of 1-3 K per day for SVC with optical depths in the range of 0.01 to 0.03. McFarquhar et al. (2000) also used the Heymsfield (1986) data, plus the in situ microphysical aircraft measurements of Booker and Stickel (1982) and estimates of the SVC optical depth from the lidar on the NASA ER-2 aircraft during the CEPEX field study in 1993 as input into the Fu and Liou (1993) δ-four-stream radiative transfer code. Estimated heating rates of 1-2 K per day for SVC with optical depths of approximately 0.01 were determined. Comstock et al. (2002) used estimates of cloud optical depth and cloud base and top heights from surface lidar measurements on Nauru Island as input into the Fu and Liou (1993) code and estimated heating rates of approximately 3 K per day for a single SVC layer with an optical depth of 0.022.

As a further test of the heating rates determined in this paper we computed IR and solar radiative heating rates for clear skies and for two SVC cloudy-sky cases using the Rapid Radiative Transfer Model (RRTM; Mlawer and Clough, 1997; Mlawer et al., 1997). RRTM uses a correlated-k method for gaseous absorption, the Clough Kneizys Davies (CKD) 2.4 water vapor continuum model (Clough et al., 1989), and cloud ice parameterizations based on an effective size and water content (Fu et al., 1998; Fu, 1996). The key model input parameters relevant to this study are the vertical profiles of atmospheric temperature, ozone, water vapor, and cloud microphysical properties

including the ice water path and a generalized effective diameter for ice (D_{ge}, e.g., eqs. 3.11-3.12, Fu, 1996).

The vertical profiles of ozone, water vapor, and temperature are provided by the Cryogenic Frostpoint Hygrometer (CFH; Vömel et al., 2007) and ECC ozonesonde launched from the Juan Santamaria Airport in Alajuela, Costa Rica at 17 Z on 25 July 2007 (Selkirk et al., 2010). The water vapor measurements extend up to about 60 mb, whereas the ozone and temperature measurements go to 10 mb. Above these levels, data from the nearest overpass of the Microwave Limb Sounder (MLS) are used. The solar zenith angle was set to 28°. For these RRTM model runs the cloud optical depth, tau, was set to zero for the clear sky case, and to 0.02 and 0.05 for the cloud cases to span the 0.0342 mean optical depth of the SVC sampled in this study. The cloud was distributed over a layer 0.5 km thick for both cloud cases. Since we did not have microphysical measurements of the SVC on 25 July 2007 the effective radius, r_e, was set to 14 μm (D_{ge} = 21 μm) in the calculations, corresponding to the value found by in situ measurements of an SVC sampled by the WB-57 aircraft on 6 August 2007 during TC4 (Davis et al, 2010, this issue).

Figure 9 shows the solar and IR heating rates determined for these three cases. The calculated solar heating rates (Figure 9a) for the 0.02 and 0.05 optical depth cloud cases are 0.23 K day^{-1} and 0.37 K day^{-1}, respectively, showing the minimal effect of the SVC on the solar radiation. On the other hand, the calculated IR heating rates (Figure 9b) for the 0.02 and 0.05 optical depth cloud cases are 0.95 K day^{-1} and 2.6 K day^{-1}, respectively. While still not large, this heating is significant compared to the clear sky case that has a slight IR cooling rate of -0.21 K day^{-1}. These calculated heating rates are not expected to

455 be exactly the same as our measured values because of our lack of in situ microphysical
456 measurements of the SVC on the 25 July, however, these calculated values are
457 comparable to the negligible solar heating rate and the 2.5-3.24 K day^{-1} IR heating rates
458 determined in this paper.
459
460 **7. Summary**
461 In this paper we determined the infrared and solar heating rates of a tropical
462 subvisible cirrus cloud through direct measurements of the net IR and solar irradiances
463 above, below, and through the cloud. The measurements were made from the NASA ER-
464 2 aircraft as it performed a rare descent profile down through an SVC layer off the east
465 coast of Nicaragua on 25 July 2007 during the TC4 field study. The ER-2 lidar
466 measurements showed that the variable SVC layer was located near the bottom of the
467 tropopause at approximately 13-15 km with mostly clear skies underneath. Its midvisible
468 optical depth varied from 0.01-0.1 with a mean of 0.0342 and a standard deviation of
469 0.0328. Its depolarization ratio was approximately 0.4, indicative of ice clouds. The
470 solar heating rate was found to be negligible, however, the infrared heating rate of the
471 SVC was determined to be approximately 2.50-3.24 K day^{-1}. These values were found to
472 be consistent with previous indirect observations of other SVC and with model-generated
473 heating rates of SVC with similar optical depths.
474 This direct measurement study therefore supports the current estimates that the
475 typical heating rate of the SVC is a few K per day with most of the heating occurring in
476 the IR. As discussed in Gage et al. (1991) heating of this magnitude can modify the
477 dynamics of the upper troposphere and lower stratosphere by increasing upward vertical

478 motions, consequently affecting stratosphere-troposphere exchange (Corti et al., 2006),
479 and possibly contributing to the dehydration of the lower stratosphere (Jensen et al.,
480 1996b), or leading to an increase in water vapor in the lower stratosphere as suggested by
481 the model simulations of Rosenfield et al. (1998). This heating is also sufficient to either
482 warm the cloud, causing it to dissipate, or drive upward motion that lifts the cloud and
483 causes it to persist for days (Jensen et al., 1996a). It has also been suggested by two
484 recent studies (Durran et al., 2009; Dinh et al., 2009), that IR heating of a few K per day,
485 as measured in this paper, may thermally force a mesoscale circulation that maintains the
486 SVC, as long as the ice crystals in the cloud have an initial mean radius that is less than 5
487 μm.
488 To address these uncertainties, and to truly determine the properties of subvisible
489 cirrus and their effects on the thermodynamic structure of the upper troposphere, on
490 stratosphere-troposphere exchange, and on climate requires more comprehensive and
491 extensive measurements that include not only the radiative properties of the SVC but also
492 the microphysical properties of the cloud, their spatial extent, and the thermodynamic
493 state of the atmosphere. This study illustrates the utility and potential of the profiling
494 sampling-strategy employed here. A high altitude aircraft that could make numerous
495 profiles through multiple subvisible cirrus equipped with solar and IR broadband and
496 spectral radiometers, a real-time cloud lidar, in situ cloud and aerosol probes, and state
497 variable sensors would finally provide a much needed comprehensive dataset for
498 characterizing both the radiative and microphysical properties of these ubiquitous tropical
499 clouds.
500

Acknowledgements

We are grateful to Warren Gore and Tony Trias from NASA Ames Research Center for their engineering and technical support during TC4, especially with the integration of the BBIR instruments into the SSFR data acquisition system on the ER-2 aircraft. This work was supported by the NASA Radiation Sciences Program under grant no. NNH07AF56I (TC4).

References

Bucholtz, A., R. T. Bluth, B. Kelly, S. Taylor, K. Batson, A. W. Sarto, T. P. Tooman, and R. F. McCoy (2008), The Stabilized Radiometer Platform (STRAP) - An Actively Stabilized Horizontally Level Platform for Improved Aircraft Irradiance Measurements, *J. Atmos. Oceanic Technol.*, *25*, 2161-2175, doi:10.1175/2008JTECHA1085.1.

Bucholtz, A., and H. Jonsson (2010), Modified Kipp & Zonen pyranometers and pyrgeometers for use on atmospheric research aircraft, *J. Atmos. Oceanic Technol.*, in preparation.

Booker, D. R., and P. G. Stickel (1982), High altitude tropical cirrus cloud observations, *Conf. on Cloud Physics Preprint*, 215-217, Amer. Meteor. Soc., Chicago, IL.

Bevington, P. R. (1969), Data Reduction and Error Analysis for the Physical Sciences, 336 pp., McGraw-Hill Co., New York, New York.

Chartrand, R. (2005), Numerical differentiation of noisy, nonsmooth data, 9 pp., Los Alamos National Laboratory, Los Alamos, NM.

Clough, S. A., et al. (1989), Line shape and the water vapor continuum, *Atmospheric Research, 23*(3-4), 229-241.

Comstock, J. M., T. P. Ackerman, and G. G. Mace (2002), Ground-based lidar and radar remote sensing of tropical cirrus clouds at Nauru island: Cloud statistics and radiative impacts, *J. Geophys. Res.*, *107* (D23), 4714-4727, doi:10.1029/2002JD002203.

Corti, T., B. P. Luo, Q. Fu, H. Vomel, and T. Peter (2006), The impact of cirrus clouds on tropical troposphere-to-stratosphere transport, *Atmos. Chem. and Phys.*, *6* (9), 2539-2547.

529 Davis, S. M., D. Hlavka, E. Jensen, K. Rosenlof, S. Schmidt, S. Borrmann, W. Frey, P.
530 Lawson, H. Voemel, and T. P. Bui (2010), In situ and lidar observations of subvisible
531 cirrus clouds during TC4, *J. Geophys. Res.*, (submitted to this special issue).
532 Dessler, A. E., S. P. Palm, W. D. Hart, and J. D. Spinhirne (2006), Tropopause-level thin
533 cirrus coverage revealed by ICESat/Geoscience Laser Altimeter System, *J. Geophys.*
534 *Res., 111*(D08), 203, doi:10.1029/2005JD006 586.
535 Dinh, T. P., D. R. Durran, and T. P. Ackerman (2009), The maintenance of tropical-
536 tropopause-layer cirrus, *J. Geophys. Res.*, submitted.
537 Durran, D. R., T. Dinh, M. Ammerman, and T. Ackerman (2009), The mesoscale
538 dynamics of thin tropical tropopause cirrus, *J. Atmos. Sci.*, in press.
539 Fu, Q., and K. N. Liou (1993), Parameterization of the radiative properties of cirrus
540 clouds, *J. Atmos. Sci., 50*, 2008-2025.
541 Fu, Q. A. (1996), An accurate parameterization of the solar radiative properties of cirrus
542 clouds for climate models, *J. of Climate, 9*(9), 2058-2082.
543 Fu, Q., P. Yang, W. B. Sun (1998), An accurate parameterization of the infrared radiative
544 properties of cirrus clouds for climate models, *J. of Climate, 11*(9), 2223-2237.
545 Gage, K. S., J. R. McAfee, D. A. Carter, W. L. Ecklund, A. C. Riddle, G. C. Reid, and B.
546 B. Balsley (1991), Long-Term Mean Vertical Motion over the Tropical Pacific:
547 Wind-Profiling Doppler Radar Measurements, *Science*, *254* (5039), 1771-1773.
548 Heymsfield, A. J. (1986), Ice Particles Observed in a Cirriform Cloud at -83°C and
549 Implications for Polar Stratospheric Clouds, *J. Atmos. Sci.*, *43*, no. 8, 851-855.

550 Immler, F., and O. Schrems (2002), LIDAR measurements of cirrus clouds in the
551 northern and southern midlatitudes during INCA (55oN, 53oS): A comparative study,
552 *Geophys. Res. Lett.*, *29*(16), 1809-1812, doi:10.1029/2002GL015077.
553 Jensen, E. J., O. B. Toon, H. B. Selkirk, J. D. Spinhirne, and M. R. Schoeberl (1996a),
554 On the formation and persistence of subvisible cirrus clouds near the tropical
555 tropopause, *J. Geophy. Res., 101*(D16), 21361-21375.
556 Jensen, E. J., O. B. Toon, L. Pfister, and H. B. Selkirk (1996b), Dehydration of the
557 upper troposphere and lower stratosphere by subvisible cirrus clouds near the tropical
558 tropopause, *Geophys. Res. Lett.*, *23*(8), 825-828.
559 Kipp & Zonen (2003), *Instruction manual CG4 pyrgeometer*, 61 pp., Kipp & Zonen,
560 Delft, Netherlands.
561 Lawson, R. P., B. Pilson, B. Baker, Q. Mo, E. Jensen, L. Pfister, and P. Bui (2007),
562 Aircraft measurements of microphysical properties of subvisible cirrus in the tropical
563 tropopause layer, *Atmos. Chem. Phys. Discuss., 7*, 6255-6292.
564 Liou, K.-N. (1980), *An Introduction to Atmospheric Radiation*, International Geophysics
565 Series, Vol. 26, 392 pp., Academic Press, Inc., San Diego, CA.
566 Mace, G. G., Q. Zhang, M. Vaughan, R. Marchand, G. Stephens, C. Trepte, and D.
567 Winker (2009), A description of hydrometeor layer occurrence statistics derived from
568 the first year of merged Cloudsat and CALIPSO data, *J. Geophys. Res., 114*,
569 D00A26, doi: 10.1029/2007JD009755.
570 McFarquhar, G. M., A. J. Heymsfield, J. Spinhirne, and B. Hart (2000), Thin and
571 subvisual tropopause tropical cirrus: Observations and radiative impacts. *J. Atmos.*
572 *Sci., 57*, no. 12, 1841-1853.

573 McGill, M., D. Hlavka, W. Hart, V. S. Scott, J. Spinhirne, and B. Schmid (2002), Cloud
574 Physics Lidar: instrument description and initial measurement results, *App. Opt., 41*,
575 no. 18, 3725-3734.
576 McGill, M.J., D.L. Hlavka, W.D. Hart, E.J. Welton, and J.R. Campbell (2003), Airborne
577 lidar measurements of aerosol optical properties during SAFARI-2000, *J. Geophys.*
578 *Res.*, *108*, doi: 10.1029/2002JD002370.
579 Mlawer, E., S. Taubman, P. Brown, M. Iacono, and S. Clough (1997), Radiative transfer
580 for inhomogeneous atmospheres: RRTM, a validated correlated-k model for the
581 longwave, *J. Geophys. Res., 102*(D14), 16663-16682.
582 Mlawer, E. J., and S. A. Clough (1997), On the extension of rapid radiative transfer
583 model to the shortwave region, *paper presented at 6th Atmospheric Radiation*
584 *Measurement (ARM) Science Team Meeting*, U.S. Department of Energy, CONF-
585 9603149.
586 Peter, T., B. P. Luo, M. Wirth, C. Kiemle, H. Flentje, V. A. Yushkov, V. Khattatov, V.
587 Rudakov, A. Thomas, S. Borrmann, G. Toci, P. Mazzinghi, J. Beuermann, C.
588 Schiller, F. Cairo, g. Di Donfrancesco, A. Adriani, C. M. Volk, J. Strom, K. Noone,
589 V. Mitev, R. A. MacKenzie, K. S. Carslaw, t. Trautmann, V. Santacesaria, and L.
590 Stefanutti (2003), Ultrathin tropical tropopause clouds (UTTCs): I. cloud morphology
591 and occurrence. *Atmos. Chem. Phys., 3*, 1083-1091.
592 Pfister, L., H. B. Selkirk, E. J. Jensen, M. R. Schoeberl, O. B. Toon, E. V. Browell, W. B.
593 Grant, B. Gary, M. J. Mahoney, T. V. Bui, and E. Hintsa (2001), Aircraft
594 observations of thin cirrus clouds near the tropical tropopause, *J. Geophys. Res.,*
595 *106*(D9), 9765-9786.

596 Philipona, R., C. Frohlich, and C. Betz (1995), Characterization of pyrgeometers and the
597 accuracy of atmospheric longwave radiation measurements, *Appl. Opt.*, *34*, 1598-
598 1605.
599 Pilewskie, P., J. Pommier, R. Bergstrom, W. Gore, S. Howard, M. Rabbette, B. Schmid,
600 P. V. Hobbs, and S. C. Tsay (2003), Solar spectral radiative forcing during the
601 Southern African Regional Science Initiative, *J. Geophys. Res., 108*(D13), 8486,
602 doi:10.1029/2002JD002411.
603 Prabhakara, C., D. P. Kratz, J. -M. Yoo, G. Dalu, and A. Vernekar (1993), Optically Thin
604 Cirrus Clouds: Radiative Impact on the Warm Pool, *J. Quant. Spectrosc. Radiat.*
605 *Transfer, 49*, no. 5, 467-483.
606 Rosenfield, J. E., D. B. Considine, M. R. Schoeberl, and E. V. Browell (1998), The
607 impact of subvisible cirrus clouds near the tropical tropopause on stratospheric water
608 vapor, *Geophys. Res. Letts., 25*(11), 1883-1886.
609 Sassen, K., M. K. Griffin, and G. C. Dodd (1989), Optical Scattering and Microphysical
610 Properties of Subvisual Cirrus Clouds, and Climatic Implications, *J. Appl. Meteor.*,
611 *28*, 91-98.
612 Sassen, K., and B. S. Cho (1992), Subvisual-Thin Cirrus Lidar Dataset for Satellite
613 Verification and Climatological Research, *J. Appl. Meteor., 31*, 1275-1285.
614 Sassen, K., and J. R. Campbell (2001), A Midlatitude Cirrus Cloud Climatology from the
615 Facility for Atmospheric Remote Sensing. Part I: Macrophysical and Synoptic
616 Properties, *J. Atmos. Sci.*, *58*, 481-496.

617 Schmidt, K. S., P. Pilewskie, B. Kindel, S. Platnick, M. King, G. Wind, G. T. Arnold, L.
618 Tian, M. Wendisch (2010), Apparent and real absorption of solar spectral irradiance
619 in heterogeneous clouds, *J. Geophys. Res.*, submitted to this special issue.
620 Selkirk, H. B., H. Vömel, J. Valverde, L. Pfister (2010), The detailed structure of the
621 tropical upper troposphere as revealed by balloonsonde observations of water vapor,
622 ozone, temperature and winds during the NASA TCSP and TC4 campaigns, *J.*
623 *Geophys. Res.*, (submitted to this special issue).
624 Uthe, E. E., and P. B. Russell (1976), Lidar Observations of Tropical High-Altitude
625 Cirrus Clouds, *IAMAP Symposium on Radiation in the Atmosphere Preprints*, 74th,
626 Garmisch-Partenkirchen, Germany.
627 Vömel, H., D. E. David, and K. Smith (2007), Accuracy of tropospheric and stratospheric
628 water vapor measurements by the cryogenic frost point hygrometer: Instrumental
629 details and observations, *J. Geophys. Res., 112*, D08305, doi:10.1029/2006JD007224.
630 Wang, P. H., P. Minnis, M. P. McCormick, G. S. Kent, and K. M. Skeens (1996), A 6-
631 year climatology of cloud occurrence frequency from Stratospheric Aerosol and Gas
632 Experiment II observations (1985-1990), *J. Geophys. Res., 101*(D23), 29 407-29 429.
633 Winker, D. M. and C. R. Trepte (1998), Laminar cirrus observed near the tropical
634 tropopause by LITE. *Geophys. Res. Letts, 25*, no. 17, 3351-3354.
635

Figure Captions:

Figure 1: The ER-2 flight track on 25 July 2007 is shown overlayed on the GOES Vis image from 16:28 UTC. The altitude profile of the ER-2 is given in the inset. The ER-2 was the sole TC4 aircraft flying on this day. (Image from NASA Langley TC4 Satellite Page: http://angler.larc.nasa.gov/tc4).

Figure 2: Profiles of (a) temperature, (b) wind direction, and (c) wind speed as measured by the ER-2 on its initial climb out over the Caribbean (red lines) and by balloonsondes launched from Alajuela, Costa Rica before (blue lines) and near the end (green line) of the flight (Selkirk et al. 2009). All three soundings in (a) show the bottom of the tropopause at approximately 15 km with a small inversion between 15-16 km. Winds were mostly out of the East (b) and were stronger below the tropopause (c).

Figure 3: The CPL attenuated backscatter signal for the entire flight on 25July2007 showing a persistent thin cirrus layer between approximately 13-15 km altitude. The thin cirrus layer occurs just below the bottom of the tropopause (see Fig. 2a). The ER-2 headings for the different flight segments over the Caribbean are also given (N=northbound; S=southbound; W=westbound). The location of the ER-2 profile through the cirrus is indicated. The white trace shows the flight track of the ER-2 as it descends and then climbs through the SVC. The flight segment corresponding to the cloud optical depths (OD) given in Figure 4a is also indicated.

Figure 4: The (a) optical depth and (b) depolarization ratio derived from the lidar data for a representative section of the thin cirrus observed on 25July2007 between 16:20-16:39 UTC (see Figure 3). The optical depth of the cirrus varies between approximately 0.01 to 0.1 with a mean of 0.0342 and a standard deviation of 0.0328. The estimated

680 with altitude indicates a constant IR heating rate through the layer. The slope of the
681 linear fit (net flux per mb pressure) is used to derive the IR heating rate
682 **Figure 9:** Calculated (a) solar and (b) IR heating rates using the RRTM radiative transfer
683 code for clear skies and two idealized subvisible cirrus cloud cases, one with a cloud
684 optical depth, tau, of 0.02, and the other with a cloud optical depth of 0.05. The cloud
685 thickness for each case was set to 0.5 km. Vertical profiles of atmospheric temperature,
686 ozone, and water vapor from balloonsondes launched from Costa Rica on 25 July 2007,
687 and cloud microphysical information from measurements of an SVC sampled on 6
688 August 2009 during TC4 are used in the calculations.
689
690

690 **Figures:**

691

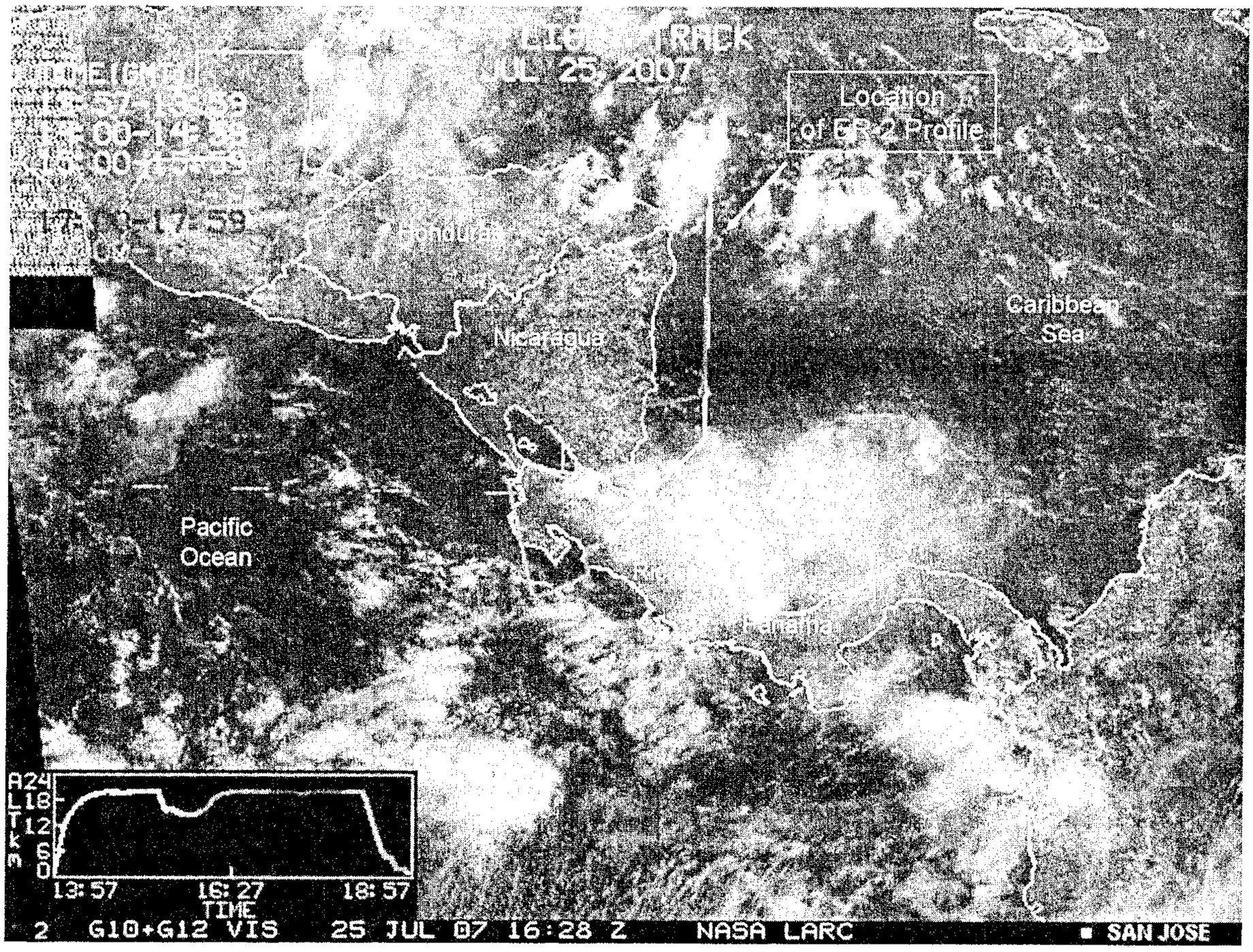

692
693
694
695

696 **Figure 1:** The ER-2 flight track on 25 July 2007 is shown overlayed on the GOES Vis
697 image from 16:28 UTC. The altitude profile of the ER-2 is given in the inset. The ER-2
698 was the sole TC4 aircraft flying on this day. (Image from NASA Langley TC4 Satellite
699 Page: http://angler.larc.nasa.gov/tc4).
700
701
702

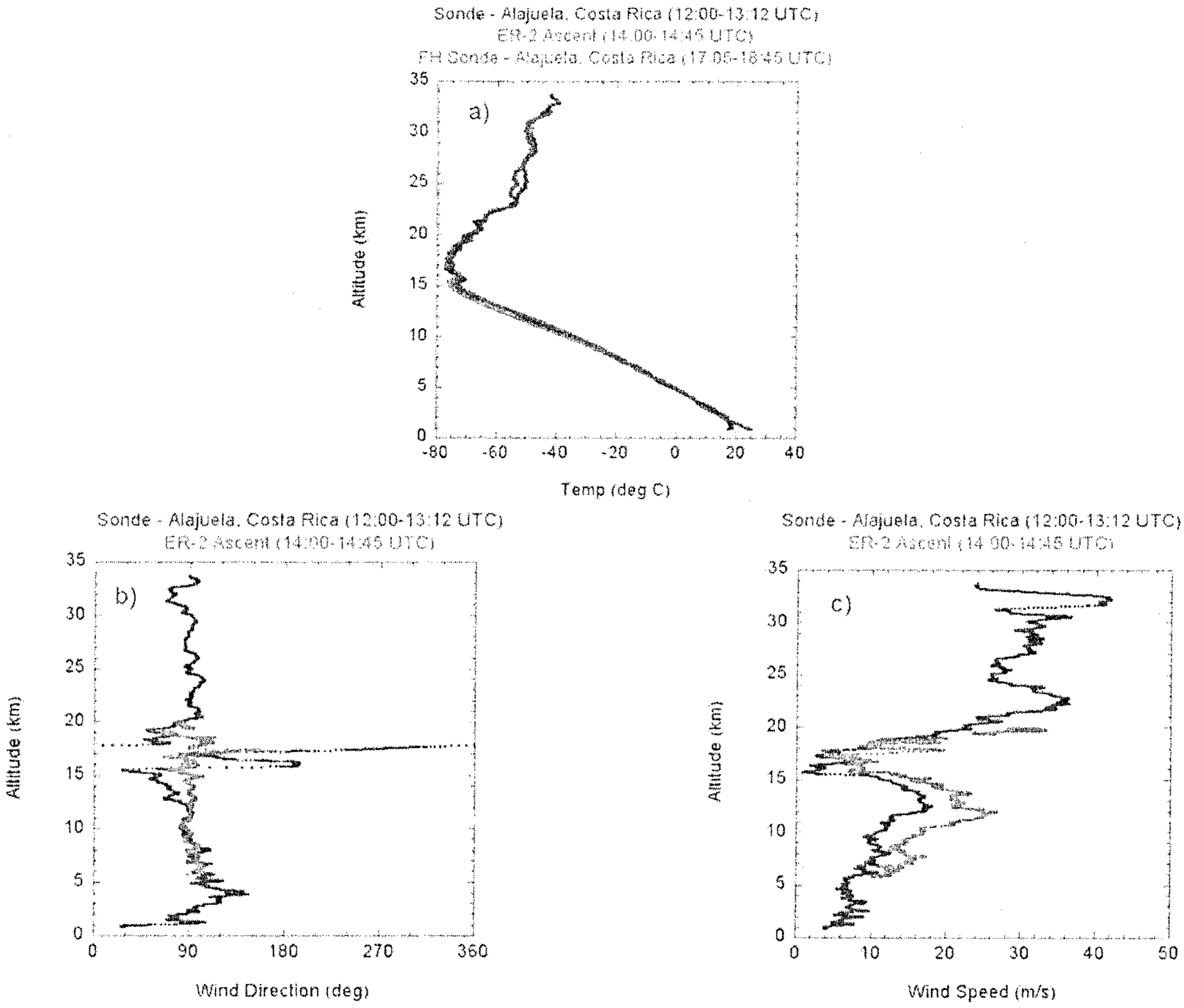

Figure 2: Profiles of (a) temperature, (b) wind direction, and (c) wind speed as measured by the ER-2 on its initial climb out over the Caribbean (red lines) and by balloonsondes launched from Alajuela, Costa Rica before (blue lines) and near the end (green line) of the flight (Selkirk et al. 2009). All three soundings in (a) show the bottom of the tropopause at approximately 15 km with a small inversion between 15-16 km. Winds were mostly out of the East (b) and were stronger below the tropopause (c).

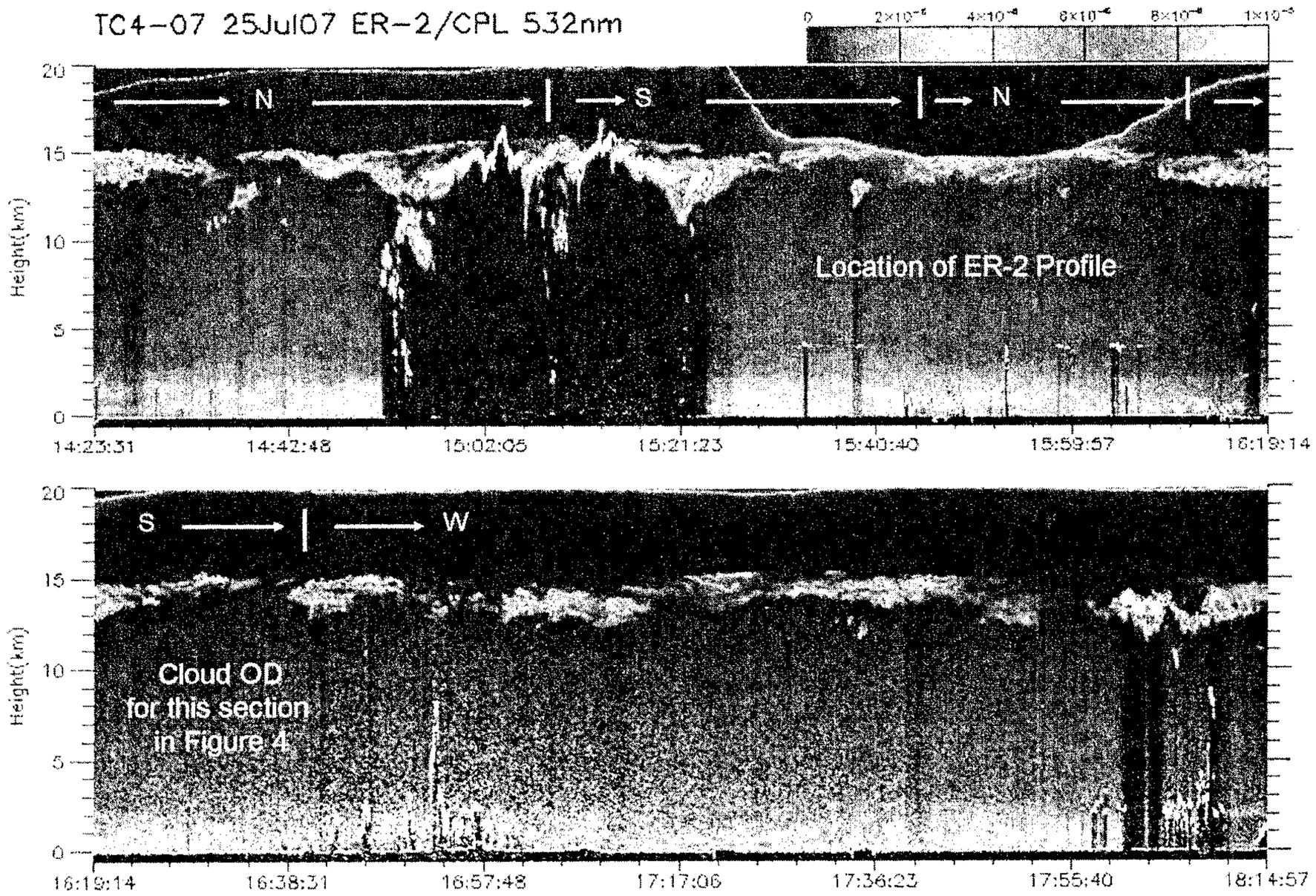

714
715
716
717 **Figure 3:** The CPL attenuated backscatter signal for the entire flight on 25July2007
718 showing a persistent thin cirrus layer between approximately 13-15 km altitude. The thin
719 cirrus layer occurs just below the bottom of the tropopause (see Fig. 2a). The ER-2
720 headings for the different flight segments over the Caribbean are also given
721 (N=northbound; S=southbound; W=westbound). The location of the ER-2 profile
722 through the cirrus is indicated. The white trace shows the flight track of the ER-2 as it
723 descends and then climbs through the SVC. The flight segment corresponding to the
724 cloud optical depths (OD) given in Figure 4a is also indicated.
725
726
727

727

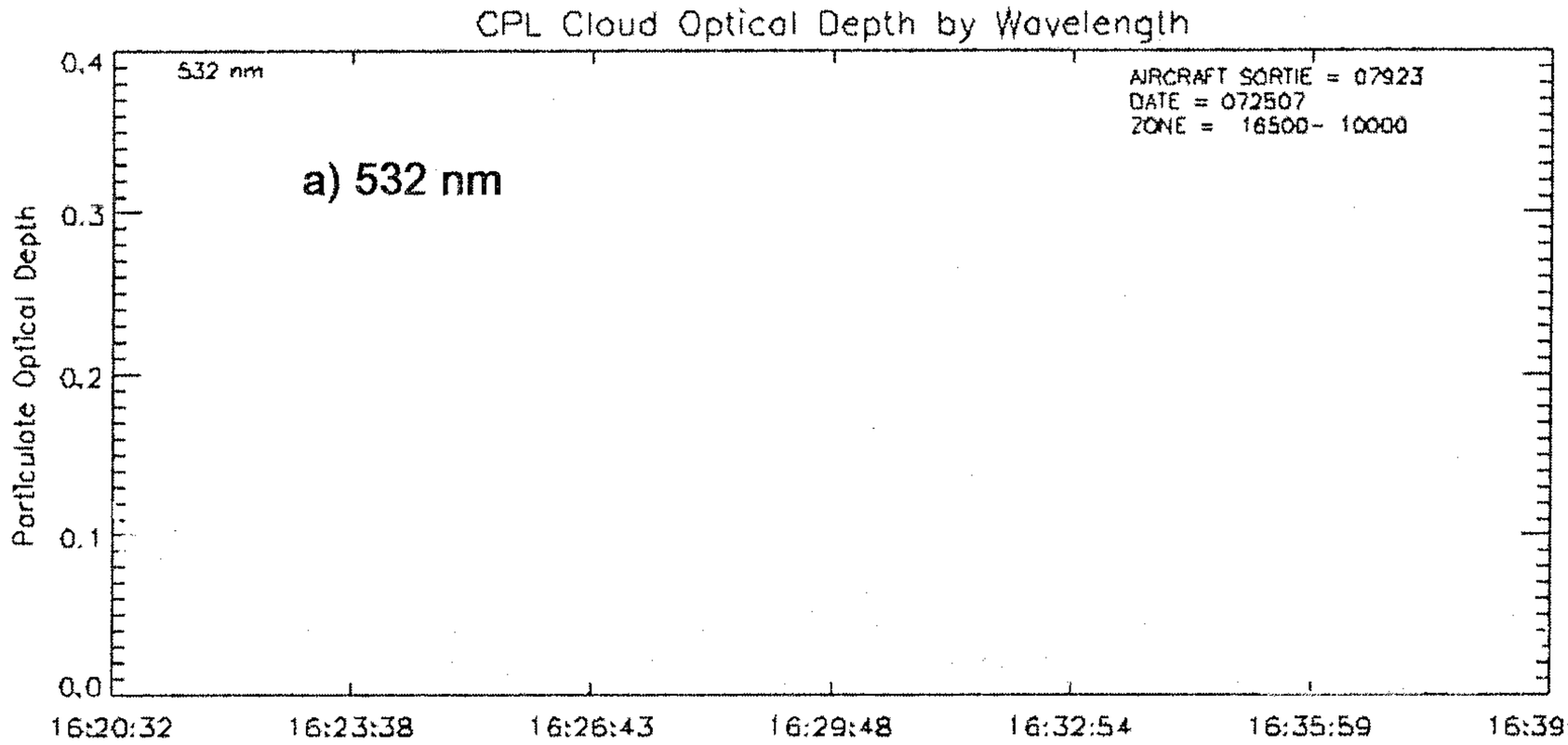

728

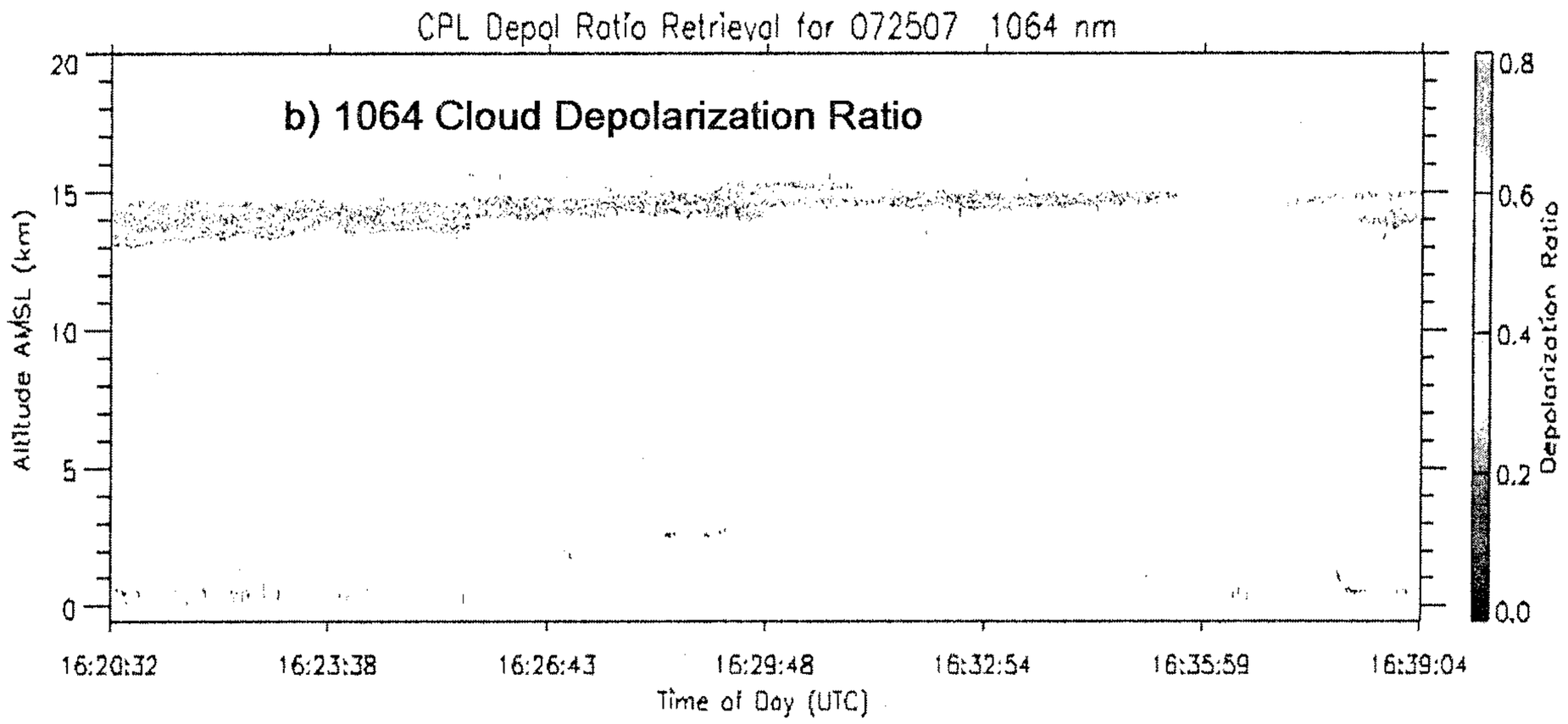

729
730
731 **Figure 4:** The (a) optical depth and (b) depolarization ratio derived from the lidar data
732 for a representative section of the thin cirrus observed on 25July2007 between 16:20-
733 16:39 UTC (see Figure 3). The optical depth of the cirrus varies between approximately
734 0.01 to 0.1 with a mean of 0.0342 and a standard deviation of 0.0328. The estimated
735 threshold for visual observation is 0.03. The depolarization ratio (b) for these clouds is
736 approximately 0.4 indicative of ice clouds.
737
738
739
740

740

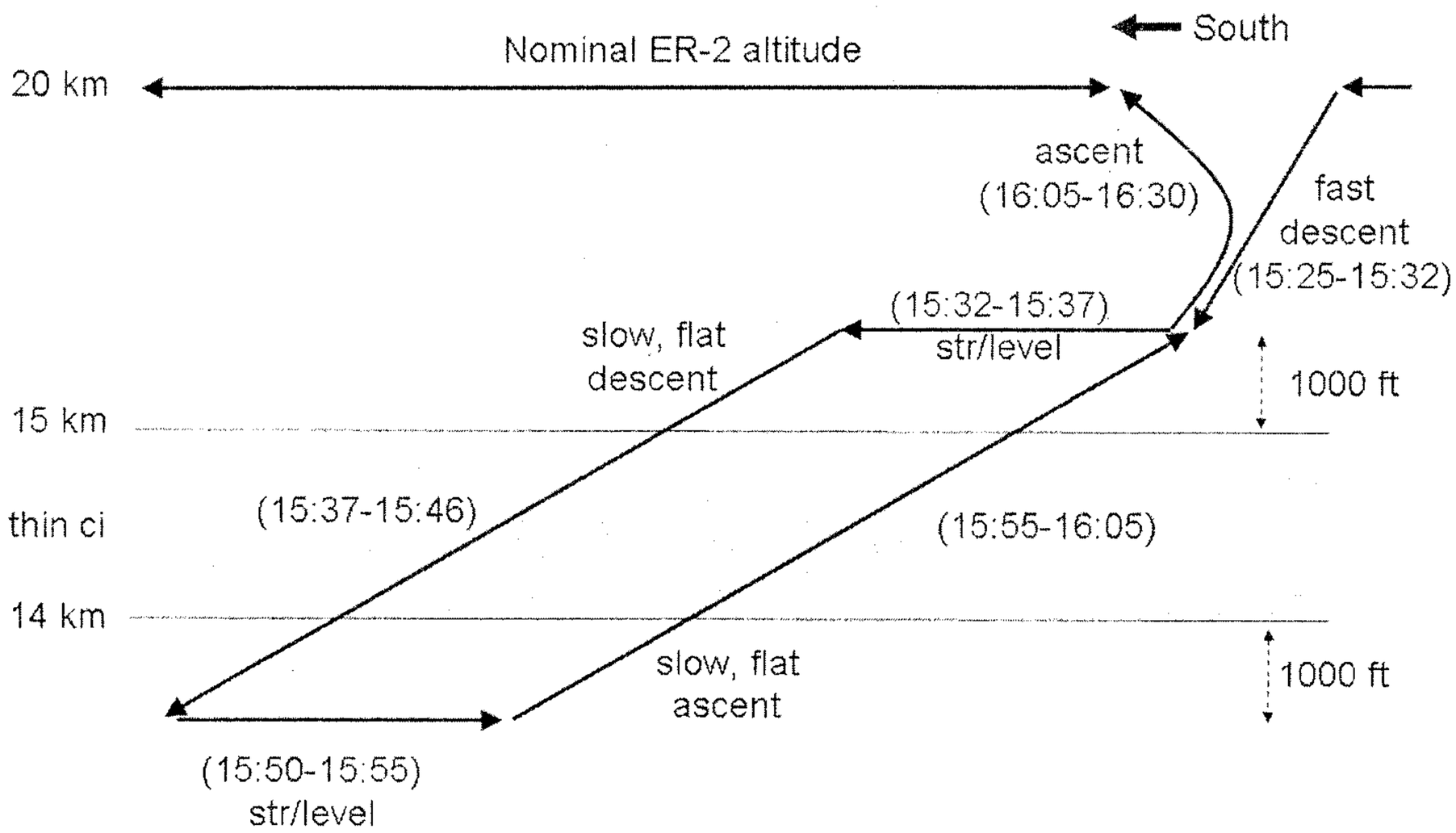

741
742

743 **Figure 5:** An idealized schematic of the flight profile flown by the ER-2 to sample the
744 subvisible cirrus layer. This flight pattern provided a level leg above and below the
745 cloud, and a descent and ascent through the cloud to measure the IR and solar broadband
746 net irradiances throughout the profile from which the heating rates were derived. The
747 UTC flight times of each leg are given. The altitudes given are approximate. The actual
748 flight pattern is shown by the white trace in Fig. 3.
749
750
751
752

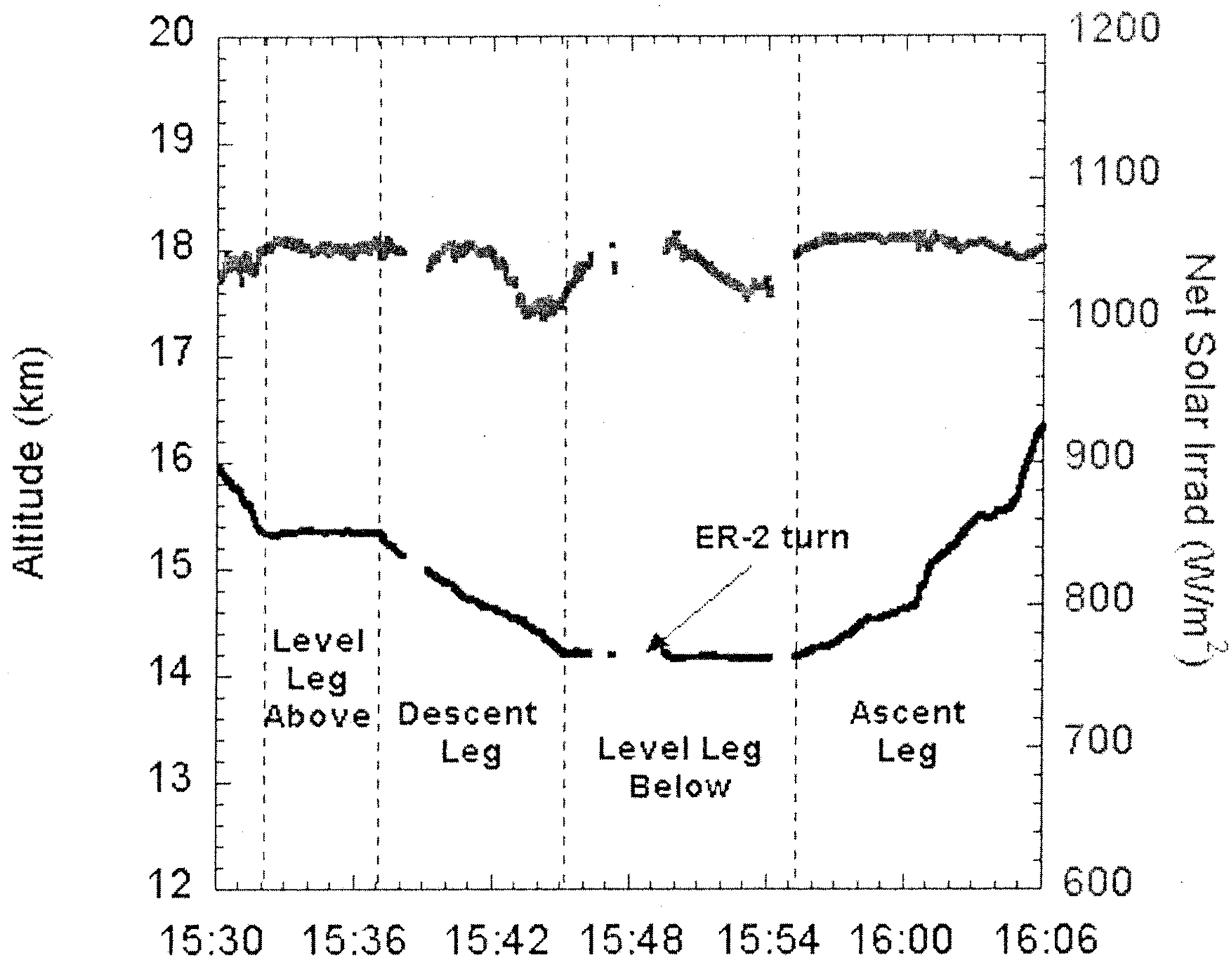

Figure 6: The net solar irradiances measured during the ER-2 profile through the subvisible cirrus and the corresponding altitudes of each leg. The net solar irradiance data for this time segment have been normalized to a solar zenith angle of 24.162° and corrected for the attitude (pitch, roll, and heading) of the aircraft. The measurements during the 180° turn of the ER-2 near 15:48 UTC have been filtered out. The dips in net irradiance at approximately 15:43 and 15:53 correspond to lower level clouds below the cirrus.

Tuesday, May 18, 2010

780

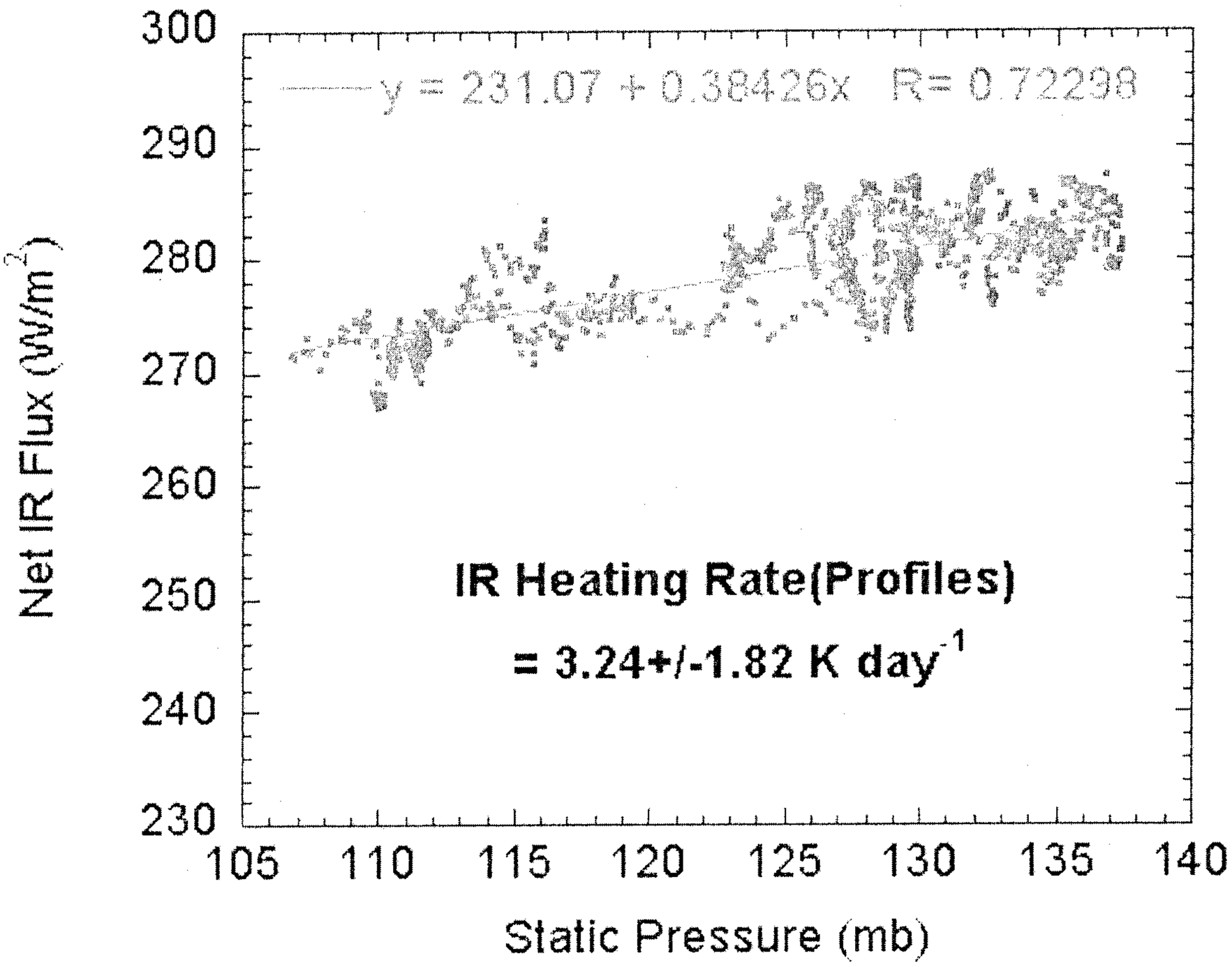

781
782
783 **Figure 8:** The net IR fluxes as a function of pressure for the descent and ascent of the
784 ER-2 through the thin cirrus layer are combined here. The linear decrease in the net flux
785 with altitude indicates a constant IR heating rate through the layer. The slope of the
786 linear fit (net flux per mb pressure) is used to derive the IR heating rate
787
788
789

789

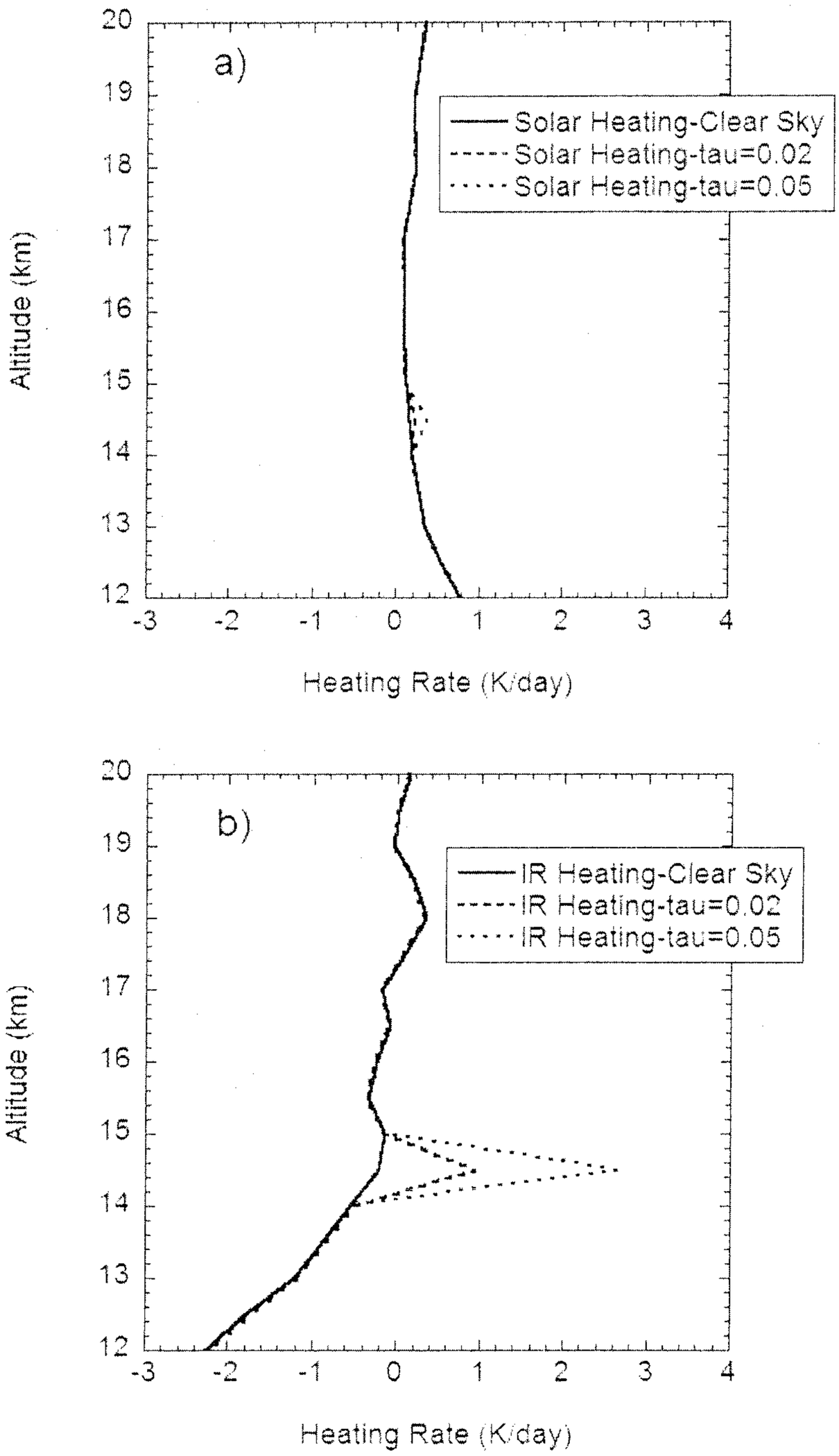

790
791

792
793

794 **Figure 9:** Calculated (a) solar and (b) IR heating rates using the RRTM radiative transfer
795 code for clear skies and two idealized subvisible cirrus cloud cases, one with a cloud
796 optical depth, tau, of 0.02, and the other with a cloud optical depth of 0.05. The cloud
797 thickness for each case was set to 0.5 km. Vertical profiles of atmospheric temperature,
798 ozone, and water vapor from balloonsondes launched from Costa Rica on 25 July 2007,
799 and cloud microphysical information from measurements of an SVC sampled on 6
800 August 2009 during TC4 are used in the calculations.
801